DECEMBER 17 2025

Directional sound field decay analysis in a reverberation room[a)]

Marco Berzborn ; Mélanie Nolan ; Efren Fernandez Grande ; Michael Vorländer

J. Acoust. Soc. Am. 158, 4706–4720 (2025)
https://doi.org/10.1121/10.0039531

JASA ARTICLE

Directional sound field decay analysis in a reverberation room[a)]

Marco Berzborn,[1,b)] Mélanie Nolan,[2] Efren Fernandez Grande,[2] and Michael Vorländer[1]
[1]*Institute for Hearing Technology and Acoustics, RWTH Aachen University, Aachen 52074, Germany*
[2]*Departamento de Ingeniería Audiovisual y Comunicaciones, Universidad Politécnica de Madrid, Madrid 28031, Spain*

ABSTRACT:
The measurement of sound absorption in reverberation rooms is subject to a poor interlaboratory reproducibility. Among other factors, this is caused by a non-isotropic sound field during the procedure. This study investigates the directional properties of the energy decay. The analysis method is based on capturing directional energy decay curves calculated from a plane wave decomposition of the sound field. Estimators for isotropy and axial symmetry are used to quantify the distributions of incident energy during the decay process. Experimental results are presented for a reverberation room in four configurations: with and without panel diffusers and with and without an absorbing specimen. Anisotropic energy distributions are found when an absorbing specimen is mounted. Especially if none or insufficient diffusing elements are mounted, the sound field isotropy is time dependent, decreasing with time, whereas the axial symmetry increases. The phenomenon is associated with a multi-exponential decay, resulting from weakly damped axial modes and strongly damped modes at grazing incidence on the absorber. It is further supported by a strong correlation between the estimated isotropy and temporally varying instantaneous energy decay rate. Results show that the isotropy estimator's temporal evolution cannot reliably identify a regression interval for accurate absorption coefficient estimation.
 https://doi.org/10.1121/10.0039531
(Received 28 April 2025; revised 8 September 2025; accepted 15 September 2025; published online 17 December 2025)
[Editor: James F. Lynch] Pages: 4706–4720

I. INTRODUCTION

Knowledge of the absorption properties of materials is crucial in the many fields involving acoustic simulations and acoustical design. The random incidence absorption coefficient is measured as per international standard ISO 354:2003 (2003) in a reverberation room with the prerequisite of the sound field in the room being diffused. However, multiple studies showed high uncertainties in the method and a poor interlaboratory reproducibility of the results (Halliwell, 1983). The use of a reference absorber for calibration to improve the reproducibility was shown not to yield consistent and reliable results (Scrosati *et al.*, 2020). It is assumed that these problems are in part caused by a non-uniform damping of the sound field (Hunt *et al.*, 1939) and a non-diffuse sound field (Kuttruff, 2009). For a more extensive overview on the historical development of research related to the problems associated with the reverberation room method for measuring absorption, as well as remaining challenges, the reader is referred to Balint *et al.* (2023).

Early approaches for the quantification of the distribution and uniformity in incident energy date back to the 1950s. Pioneering the application of angular analysis of sound fields, Thiele (1953) introduced the use of an omnidirectional microphone in conjunction with a parabolic mirror for measuring directionally filtered room impulse responses. A metric was further derived, which will be referred to as directional energy variation, to quantify the isotropy of the sound field. A similar method using highly directional *shotgun* microphones was applied by Venzke and Dämmig (1961) to study the energy distribution in a reverberation room and observe anisotropic energy distributions throughout the early part of the decay process of the sound field. Gover *et al.* (2002) extended the directional energy variation estimator to microphone arrays and performed an analysis of various room types (Gover *et al.*, 2004), including a reverberation room. More recently, Nolan *et al.* (2018) and Nolan *et al.* (2020) studied the isotropy conditions of the steady state and decaying sound field in reverberation rooms using a spherical harmonic (SH) expansion of the wave number spectrum. The respective metric by Nolan *et al.* (2018), which will be referred to as monopole ratio, is calculated as the energy ratio of the SH monopole moment, which is omnidirectional and, therefore, isotropic over the total energy in all moments, which have distinct directions. Similar metrics, involving large sample tests and leveraging the same property of the SHs, were introduced by Jammalamadaka and Terdik (2019) and Sahoo *et al.* (2019)

[a)]This paper is part of a special issue on Sound Absorption and Diffusion: Modeling, Measurement and Application. Initial results were presented in "On the directional properties of energy decay curves," 23rd International Congress on Acoustics, Aachen, Germany, September 2019, and "Comparison of isotropy estimators for the analysis of reverberation rooms," E-Forum Acusticum, Lyon, France, December 2020.
[b)]Email: marco.berzborn@akustik.rwth-aachen.de

https://doi.org/10.1121/10.0039531

in the fields of astrophysics and meteorology. Note that extensive research has been performed on the quantification of uniformity of distributions on the sphere in the sciences, and interested readers are referred to a review paper by García-Portugués and Verdebout (2018).

Theoretical work by Hunt *et al.* (1939) and Kuttruff (1958) highlighted the absorbing sample's influence on the sound field's decay process, leading to multi-exponential energy decay curves (EDCs). Meyer and Diestel (1952) investigated the influence of the absorbing specimen on the energy decay using line arrays of microphones and loudspeakers, measuring EDCs while exciting and capturing the sound field only with respect to specific directions. Berzborn and Vorländer (2021) suggested the calculation of directional energy decay curves (DEDCs) based on the decomposition of the sound field using a microphone array and calculated the isotropy of the sound field during its decay based on the directional energy variation. Other metrics and estimators to quantify sound field diffuseness based on microphone array measurements, not limited to the analysis of reverberation rooms, have been proposed by Pulkki (2007), Epain and Jin (2016), and Herzog and Habets (2021).

In this work, we present a detailed analysis of the angular distributions of incident energy during the sound field decay in a reverberation room involving the DEDC framework. Measurements are performed in the room in four different configurations: the empty room equipped with and without panel diffusers, and including a highly absorptive glass wool sample, again, equipped with and without panel diffusers. Based on a SH decomposition of the DEDC, the monopole ratio estimator is applied to quantify the isotropy condition. Additionally, a second estimator for axial symmetry in the incident energy is introduced based on the work by Jammalamadaka and Terdik (2019). Finally, we discuss the consequences of nonuniform damping and the resulting existence of directionally dependent multi-exponential sound field decay on the temporal evolution of the symmetry estimators.

The paper is structured as follows: Section II introduces the sound field decomposition and DEDC frameworks using a spherical microphone array. Section III introduces quantification methods for the symmetry of energy distributions, as well as a method to reconstruct DEDCs which are subject to specific symmetries only. Section IV details the experimental setup in a reverberation room in different configurations with varying degrees of sound field isotropy. The results are presented in Sec. V, followed by a discussion in Sec. VI and the conclusions are provided in Sec. VIII.

II. DIRECTIONAL SOUND FIELD DECAY ANALYSIS

A. Sound field decomposition

Spherical microphone arrays allow for the capture of directional room impulse responses (DRIRs), retaining directional information about the sound field in the room (Rafaely, 2015). A DRIR measured with a spherical microphone array can be written as vector $\mathbf{p}(k) \in \mathbb{C}^{L\times 1}$ of L pressure sensor signals such that

$$\mathbf{p}(k) = [p(k, r_1, \mathbf{\Omega}_1), \ldots, p(k, r_L, \mathbf{\Omega}_L)]^{\mathrm{T}}, \tag{1}$$

where r_l is the radius and $\mathbf{\Omega}_l = (\theta_l, \phi_l)$ is a vector containing the colatitude and azimuth angles of the lth sensor position, respectively, k is the wave number, and $(\cdot)^{\mathrm{T}}$ denotes the transpose operator. Assuming a plane wave sound field, the sound field can be decomposed into a continuum of the latter. In a first step, the spherical wave spectrum vector $\mathbf{a_{nm}}(k) \in \mathbb{C}^{(N+1)^2\times 1}$ is calculated for a maximum SH order N by solving (Williams, 1999)

$$\mathbf{a_{nm}}(k) = \mathbf{B}^{\dagger}(k)\mathbf{p}(k), \tag{2}$$

where $\mathbf{B}^{\dagger} \in \mathbb{C}^{(N+1)^2\times L}$ denotes the regularized pseudo-inverse of the combined modal strength and SH basis matrices defining the spherical array geometry as defined by Rafaely (2015). Note that the bold indices $(\cdot)_{\mathbf{nm}}$ indicate that the vector contains the SH coefficients for orders n and degrees m up to a maximum truncation order N. The modal strength functions describe the radial propagation of purely traveling plane waves in spherical coordinates. As a consequence, evanescent waves are not considered in the decomposition.

The inverse Fourier transform of the spherical wave spectrum is also referred to as the spherical harmonic domain directional room impulse response (SH-DRIR). In a second step, the spherical wave spectrum is projected onto a grid of Q steering directions yielding the plane wave density vector $\mathbf{a}(k) \in \mathbb{C}^{Q\times 1}$, also referred to as the two-dimensional wave number spectrum in the spatial domain (Rafaely, 2015),

$$\mathbf{a}(k) = \mathbf{Y}\mathbf{W_{nm}}\mathbf{a_{nm}}(k). \tag{3}$$

The matrix $\mathbf{Y} \in \mathbb{R}^{Q\times(N+1)^2}$ is the steering matrix of the array

$$\mathbf{Y} = \left[\mathbf{y_1^{\mathrm{T}}}, \mathbf{y_2^{\mathrm{T}}}, \ldots, \mathbf{y_Q^{\mathrm{T}}}\right]^{\mathrm{T}}, \tag{4}$$

containing $q \in (1, \ldots, Q)$ steering vectors

$$\mathbf{y}(\mathbf{\Omega}_q) = \left[Y_0^0(\mathbf{\Omega}_q), Y_1^{-1}(\mathbf{\Omega}_q), \ldots, Y_N^N(\mathbf{\Omega}_q)\right], \tag{5}$$

where $Y_n^m(\mathbf{\Omega}_q)$ are the respective SH basis functions evaluated at $\mathbf{\Omega}_q$. The matrix $\mathbf{W_{nm}} \in \mathbb{R}^{(N+1)^2\times(N+1)^2}$ is a diagonal matrix containing Dolph-Chebyshev weights (Rafaely, 2015) for uniform sidelobe attenuation. Applying the inverse Fourier transform, the time domain plane wave amplitude density is calculated as $\mathbf{a}(t) = \mathcal{F}^{-1}\{\mathbf{a}(k)\}$, which is to be interpreted as the angular-temporal distribution of plane waves impinging on the receiver.

B. Directional energy decay function

Analogous to the integral definition of the EDC, we define the DEDC by performing the integration by

Schroeder (1965) on the time domain amplitude density function from Eq. (3). The definition of the DEDC is given by

$$\mathbf{d}(t) = \int_t^\infty |\mathbf{a}(\tau)|^2 \mathrm{d}\tau = \mathbf{e_s} - \int_t^\infty |\mathbf{a}(\tau)|^2 \mathrm{d}\tau, \tag{6}$$

where $\mathbf{e_s}$ is the vector of steady-state energies in discrete directions $\mathbf{\Omega}_q$. $\mathbf{d}(t)$ and $\mathbf{e_s}$ are real-valued vectors $\in \mathbb{R}^{Q\times 1}$. In contrast to the directional analysis of sound fields purely based on DRIRs, which may only give information about the directional distribution of energy for a single instance in time, the analysis of the DEDC provides directional information about the energy decay process and, accordingly, the angular distribution of the remaining energy for each time instance. Consequently, it allows to reveal nonuniform energy decays and highlight directions with dominant energy incidence.

C. Temporal truncation

Because the measured DRIR and, thus, the DEDC are subject to sensor noise, the infinite integration in Eq. (6) needs to be limited. A number of methods have been proposed or standardized for the truncation of omnidirectional EDCs (Guski and Vorländer, 2014). Methods which do not assume a strictly single-exponential decay function can be adapted to DEDC truncation without modification. In the present work, we estimate the truncation limit as the time at which DEDC and the noise power are equal using the algorithm proposed by Lundeby *et al.* (1995). Subsequently, the DEDCs are truncated at a decay level corresponding to a 20 dB headroom above the noise power at the intersection time. The required headroom level is dependent on the accuracy of the intersection time estimation. An increased headroom is chosen to counteract increased uncertainty caused by the presence of multi-exponentially decaying DRIRs. To ensure joint valid time intervals for all directions of incidence, the DEDC is finally truncated to the shortest truncation time.

D. Instantaneous decay rate

Kuttruff (1958) theoretically showed that the gradient of the logarithm of the omnidirectional EDC at $t = 0$ is proportional to the energy weighted average damping of all modes constituting the sound field. Analogously, we may define the instantaneous decay rate, which is inversely proportional to the dominant damping of the EDC, at any given time during the decay as

$$\gamma(t) = -\frac{1}{60}\frac{\mathrm{d}}{\mathrm{d}t} 10\ \log_{10} e(t), \tag{7}$$

which has the unit $1/\mathrm{s}$ and is inversely proportional to reverberation time. Strictly speaking, the unit would be $60\ \mathrm{dB}/\mathrm{s}$ as per the definition of the reverberation time.

The omnidirectional EDC $e(t)$ is calculated as the Schroeder (1965) integral of the squared monopole moment of the SH-DRIR $a_{00}(t)$; cf. Eq. (2). For $t = 0$, this is equivalent to the expression defined by Kuttruff (1958). If all modes constituting the sound field are dampened approximately equally, the instantaneous decay rate is constant and equal to the reciprocal of the reverberation time obtained according to ISO 354:2003 (2003). For multi-exponential decay functions, the instantaneous damping is a monotonically decreasing function of time. It is important to note that the instantaneous decay rate cannot be used to identify the individual damping constants of multi-exponential decay processes as it only provides information about the apparent rate of change in damping at a specific time. In fact, in some cases, the instantaneous decay rate may never be equal to the one or more of the true damping constants of the modes constituting the sound field.

As the EDC typically is subject to instantaneous temporal energy fluctuations, its gradient is not a smooth function. Hence, smoothing is required before the gradient is calculated. In the present work, a Savitzky-Golay smoothing filter is applied for simultaneous smoothing and gradient estimation (Savitzky and Golay, 1964). The length of the smoothing filter is calculated as $T_{20}/12$, which is inspired by the smoothing filter recommendations for the direct EDC measurement method using stochastic noise and is suitable for this application.

III. SYMMETRY ANALYSIS

For further in-depth analysis and quantification of the directionality of the sound field, the DEDCs can be projected into a SH basis. The respective spherical harmonic domain directional energy decay curve (SH-DEDC) is defined as

$$\mathbf{d_{nm}}(t) = \tilde{\mathbf{Y}}^\dagger \mathbf{d}(t), \tag{8}$$

where $\tilde{\mathbf{Y}}^\dagger$ is the pseudo-inverse of the SH basis matrix $\tilde{\mathbf{Y}}$ of order $\tilde{N}$ evaluated for the Q steering directions. This definition is analogous to the steering matrix in Eq. (4) but not limited to the same SH order. Instead, an increased SH order $\tilde{N} > 2N$ should be used as the order is increased by a factor of 2 in Eq. (6). The SH order is bounded according to the sampling theorem, which requires the number of steering directions to be at least equal to the number of SH coefficients. In this work, the maximum order is chosen such that the condition number of the SH basis matrix does not exceed a value of 1.1. This results in a maximum order of $\tilde{N} = 30$, which far exceeds the minimum required order. Note that the threshold for the condition number of the SH basis matrix is chosen arbitrarily but ensures a stable inversion and a valid orthonormal transform (Zotter, 2009). Alternatively, the required SH order can be found iteratively by imposing a maximum allowed error in the reconstruction of the DEDC based on the SH-DEDC.

https://doi.org/10.1121/10.0039531

A. Full spherical symmetry

Following the definition of a diffuse sound field, the DEDC should be independent of the direction of incidence, that is, the magnitude of the DEDC should be uniformly distributed over the two-sphere for each time instance. For such a uniform distribution on the two-sphere, the SH-DEDC is only described by its monopole moment $Y_0^0(\mathbf{\Omega})$ (Nolan *et al.*, 2018); see Fig. 1.

Analogous to the method proposed by Nolan *et al.* (2018), we estimate the isotropy of sound fields as the ratio between the monopole moment of the SH-DEDC and the sum of all remaining moments such that

$$\iota_\Omega(t) = \frac{|d_{0,0}(t)|}{\sum_{n=0}^{N}\sum_{m=-n}^{n}|d_{n,m}(t)|}. \tag{9}$$

Note that in the original formulation, Nolan *et al.* (2018) used the magnitude of the wave number spectrum, which is proportional to the square root of the DEDC. Conversely, the DEDC is proportional to the energy contained in the wave number spectrum.

In the case of full spherical symmetry, the monopole moment is expected to be proportional to the EDC measured with an omnidirectional receiver $d_{0,0} \propto e(t)/\sqrt{4\pi}$ while $d_{n,m} = 0\ \forall n > 0$. Consequently, Eq. (9) equates to one in the case of an isotropic sound field and zero for a fully anisotropic sound field.

B. Axial symmetry

In fully axially symmetric sound fields, the SH-DEDC comprises only mirror-symmetric SHs, which fulfil the equality condition $d_{n,m} = d_{n,-m}$, whereas all remaining coefficients are zero (Jammalamadaka and Terdik, 2019). Moments fulfilling the axial symmetry condition are, for example, the second order harmonics highlighted in Fig. 1. Conditions under which the SH-DEDC is subject to axial symmetry are, for example, the presence of dominant axial modes or flutter echoes.

Analogous to the isotropy estimator, the axial symmetry estimator can be defined as the ratio of the magnitude sum of all axially symmetric coefficients and the summed magnitude of all coefficients such that

$$\iota_a(t) = \frac{\sum_{n=1}^{N/2}\sum_{m=-2n}^{2n}|d_{2n,m}(t)|}{\sum_{n=0}^{N}\sum_{m=-n}^{n}|d_{n,m}(t)|}. \tag{10}$$

Note that we exclude the monopole moment's magnitude from the numerator. Hence, the axial symmetry in the non-isotropic moments is quantified.

C. Partial angular reconstruction

Analogous to the estimators for spherical symmetry, energy distributions comprising only certain symmetry properties can be reconstructed from the SH-DEDCs using an adapted steering matrix $\hat{\mathbf{Y}}$, which is a sparse subset of $\tilde{\mathbf{Y}}$ with nonzero entries only for orders and degrees fulfilling the respective symmetry condition. Note that in contrast to the symmetry quantification in Secs. III A and III B, the zeroth order harmonic is included for the reconstruction. This is important for consistency in the visualization and interpretation of the energy distributions in Sec. V.

For axial symmetry, the reconstruction matrix contains reduced SH vectors of the form

$$\hat{\mathbf{y}}_\mathbf{q} = \left[Y_0^0(\mathbf{\Omega_q}), 0, 0, 0, Y_2^{-2}(\mathbf{\Omega_q}), 0, \ldots, Y_{\tilde{N}}^{\tilde{N}}(\mathbf{\Omega_q})\right]. \tag{11}$$

The axially symmetric reconstruction of the DEDCs is then given by

$$\hat{\mathbf{d}}(t) = \hat{\mathbf{Y}}\mathbf{d_{nm}}(t). \tag{12}$$

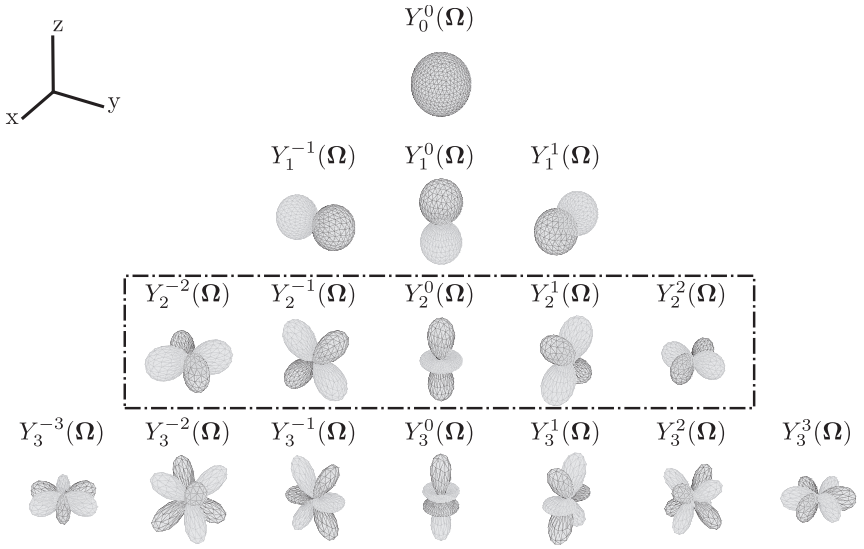

FIG. 1. Real-valued SH basis functions up to third order. Black line segments and gray segments represent positive and negative phase responses, respectively. The frame indicates coefficients fulfilling the axial symmetry condition.

Analogously, the reconstruction matrix for non-axially symmetric DEDCs contains zero entries for all coefficients fulfilling the axial symmetry condition, again, including the zeroth order harmonic for consistent visualization.

IV. EXPERIMENTAL SETUP

The DEDCs were analyzed experimentally in a rectangular reverberation room at the Technical University of Denmark (2800 Kgs. Lyngby, Denmark) in four configurations: the empty room, with and without panel diffusers, and room occupied with an absorbing sample of glass wool (Ecophon Industry Modus S with a thickness of 100 mm and a surface area of 10.8 m^2; Hyllinge, Sweden), again, including and excluding panel diffusers. The dimensions of the room are $(L_x, L_y, L_z) = (6.25\ \text{m}, 7.85\ \text{m}, 4.9\ \text{m})$ with an approximate volume of 245 m^3, resulting in a Schroeder frequency slightly above 300 Hz. A numerically calculated finite-size random incidence absorption coefficient for the relevant frequency bands is given in Table I. See Appendix A for additional information on the calculation method. The absorption coefficient exceeds one as a result of edge effects and increased absorbing area from the exposed sides of the specimen, which lack a frame. Omitting the frame mitigates sound field scattering and the corresponding presence of near-field sources in proximity to the microphone array. The sound field in the room was excited by a source mounted in a corner below the ceiling at approximately $(0.2\ \text{m}, 0.2\ \text{m}, 4.7\ \text{m})$; cf. Fig. 2. The impulse response measurement was performed with the ITA-Toolbox (Berzborn *et al.*, 2017) using exponential sweeps as excitation signal. Signal acquisition was performed using a National Instruments NI USB-4431 DAQmx system (Austin, TX).

A UR5 (Universal Robots, Odense, Denmark) scanning robot arm in combination with a pressure-field 1/2 in. Brüel and Kjær type 4192 microphone paired with a Brüel and Kjær Nexus pre-amplifier (Virum, Denmark) was used to sample a sequential dual-layer spherical microphone array; cf. Fig. 2. The microphone was mounted on an extension rod to reduce the influence of the robotic arm on the captured sound field. Three different microphone array positions were used; cf. positions R_1–R_3 in Fig. 2. Position R_1 is approximately centered above the absorber, position R_2 is offset but still above the absorbing specimen, and position R_3 is located next to the absorber.

The two layers of the array with radii $r = (0.25\ \text{m}, 0.45\ \text{m})$ consist of 144 sampling positions chosen according to an equal-area grid on the sphere (Leopardi, 2006). Additional sampling positions inside the respective spheres were used to stabilize the eigenfrequencies of the spheres (Chardon *et al.*, 2015). The resulting virtual array consists of 310 sampling positions. A total of three receiver array positions were used, as indicated in Fig. 2. For a full sequential array, the measurement duration ranged from 2.5 to 4.5 h, depending on the presence of an absorbing sample. The temperature was logged before and after each measurement. Temperature changes remained well below 0.3 °C during the measurement of one sequential array. Correlation analysis between additional co-located room impulse responses measured before and after scanning of a sequential array indicated good agreement for all presented results. The fully automated sampling approach provides a high signal-to-noise ratio and prevents microphone mismatch while minimizing potential positioning errors.

TABLE I. Finite-size random incidence absorption coefficient $\bar{\alpha}$, as well as the array configuration, used SH order N, and sidelobe attenuation in dB R.

	315 Hz	500 Hz	800 Hz	1.25 Hz
$\bar{\alpha}$	1.37	1.36	1.33	1.16
Array	Full	Full	Full	Inner
N	5	6	8	8
R	48 dB	59 dB	81 dB	81 dB

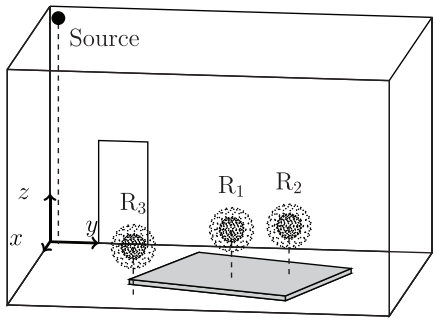

FIG. 2. Sketch of the rectangular reverberation room, including the source and receiver positions, as well as the placement of the absorbing specimen. Panel diffusers are omitted.

The DEDCs analysis and isotropy quantification were performed for third-octave bands from 250 Hz to 2 kHz, from which a selected number of frequency bands is presented here. The influence of the setup on the sound field as well as angular aliasing was found to increase above 1 kHz when all microphone positions were used. Hence, only the inner sphere was used for third-octave bands above 1 kHz.

To achieve a high signal-to-noise ratio after decomposition into plane waves, the SH order was reduced toward bands of lower frequencies. Note that this approach is comparable to manually applying regularization to an inverse problem. The Dolph-Chebyshev weights were chosen to achieve a uniform angular resolution at a main-lobewidth of 60°. The used array configuration, SH order and resulting sidelobe attenuation for each frequency band are found in Table I. A soft limiting approach, following Politis and Gamper (2017), is chosen as regularization for the inverse matrix $\mathbf{B}^{\dagger}$ to prevent signal degradation caused by noise amplification. The SH orders in Table I are chosen such that the gain limit does not affect the angular resolution of the beamformer. Finally, the plane wave decomposition is performed for 1500 steering directions chosen according to the approximately uniform partitioning of the sphere by Leopardi (2006).

The reverberation times estimated from the omnidirectional response of the array are given in Fig. 3. Note that the

https://doi.org/10.1121/10.0039531

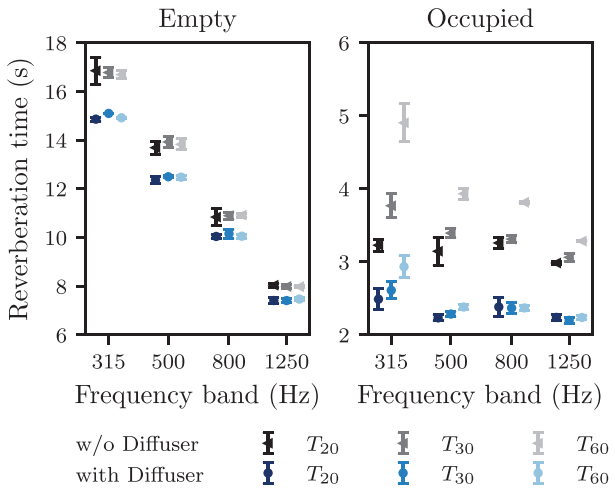

FIG. 3. Mean and standard deviation of the reverberation time estimates calculated using linear regression within the specified intervals.

EDCs were found to be decaying multi-exponentially for all frequency bands in the occupied room omitting panel diffusers, as well as for the 315 and 500 Hz frequency bands when panel diffusers are mounted.

V. RESULTS

A. Directional decay analysis

1. Angular domain

Figure 4 shows the DEDCs for the 315 Hz third-octave frequency band for all four room configurations captured at position R_1. The DEDCs are normalized by the monopole moment of the respective SH-DEDCs. Hence, the color map and contour lines in Fig. 4 represent the directional deviation from the monopole moment in dB, that is, positive values indicate a higher energy incident from respective directions compared to the monopole moment, whereas negative values indicate lower energy incident. The DEDCs are rotated such that the direction defined by colatitude and azimuth angles $(\theta, \phi) = (90°, 0°)$ aligns with the x axis as defined in Fig. 2. The energy distributions are visualized for time instances corresponding to decay levels of -5, -25, and -35 dB, which are extracted from the omnidirectional EDC. These are chosen as they bound the interval typically used for the regression of reverberation times. An analysis of the steady-state sound field is not detailed in the present study. In the following, the omnidirectional decay level will be used to indicate temporal progression as it provides a scale independent from individual reverberation times, associated with different room configurations and frequency bands. Consequently, *time* and the *omnidirectional decay level* are used interchangeably.

The two leftmost columns in Fig. 4 reveal that if no absorbing specimen is present in the room, the sound field seems to be close to isotropic at a decay level of -5 dB, as the incident energy measured in the DEDCs varies no more than ± 1.5 dB. However, at later decay levels corresponding to -25 dB and -35 dB, the DEDCs show a directionally dependent increase in incident energy, which is more pronounced for the configuration without panel diffusers. The directions of increased incident energy correspond to the directions of tangential modes in the yz-plane, i.e., azimuth angles $\pm 90°$ and colatitude angles between $0°$ and $90°$, and axial modes in the y axis, i.e., azimuth angles $\pm 90°$ and colatitude angle $90°$. The dominant maxima toward the south pole in the room without diffusers are most probably the result of model mismatches in the sound field decomposition caused by near-field effects or the presence of evanescent waves.

When the absorbing specimen is placed in the room, the sound field can no longer be considered isotropic, as illustrated in the two rightmost columns of Fig. 4. During the early decay, the incident energy measured in the DEDCs varies by more than 3 dB, specifically evident for deviations with negative sign. These variations are even more pronounced during the late part of the decay process, showing time-dependent increase in magnitude. Without panel diffusers (see the third column of Fig. 4), distinct maxima with increasing amplitude toward the late part of the decay end, observed at $\pm 90°$ azimuth, indicate sound field de-mixing. These maxima correspond to the directions of axial modes in the y axis. Hence, the sound field is primarily constituted of axial modes and far from isotropic. The increase in incident energy variation found in aforementioned directions additionally indicates a lower damping of axial modes in the y axis compared to other directions.

If the room is equipped with panel diffusers, the overall differences in magnitude are reduced (see fourth column of Fig. 4). However, the energy incident over the upper hemisphere above the absorbing specimen is again anisotropic, additionally showing a de-mixing during the decay. Although the strong axial symmetry in the y axis is no longer observed, the panel diffusers fail to sufficiently increase diffusion during the late decay. Instead, marginal axial symmetry with respect to the x axis for decay levels of -35 dB and below is found.

In the considered frequency band, the panels are neither acoustically transparent nor fully reflecting because their dimensions are approximately equal to the wave length. Seemingly, this results in complex coupling between the wave field, panel diffusers, and absorbing sample. For frequency bands above 500 Hz, the panel diffusers are found to be more effective at distributing acoustic energy, that is, configurations including diffusers show more uniform distributions of incident energy. Additional figures are part of the supplementary material. Results for the 1.25 kHz frequency band are discussed in Sec. V B.

2. Spherical harmonic domain

Figure 5 shows the SH-DEDCs at position R_1 for the 315 Hz third-octave frequency band for all room configurations. The SH-DEDCs are depicted for orders greater or

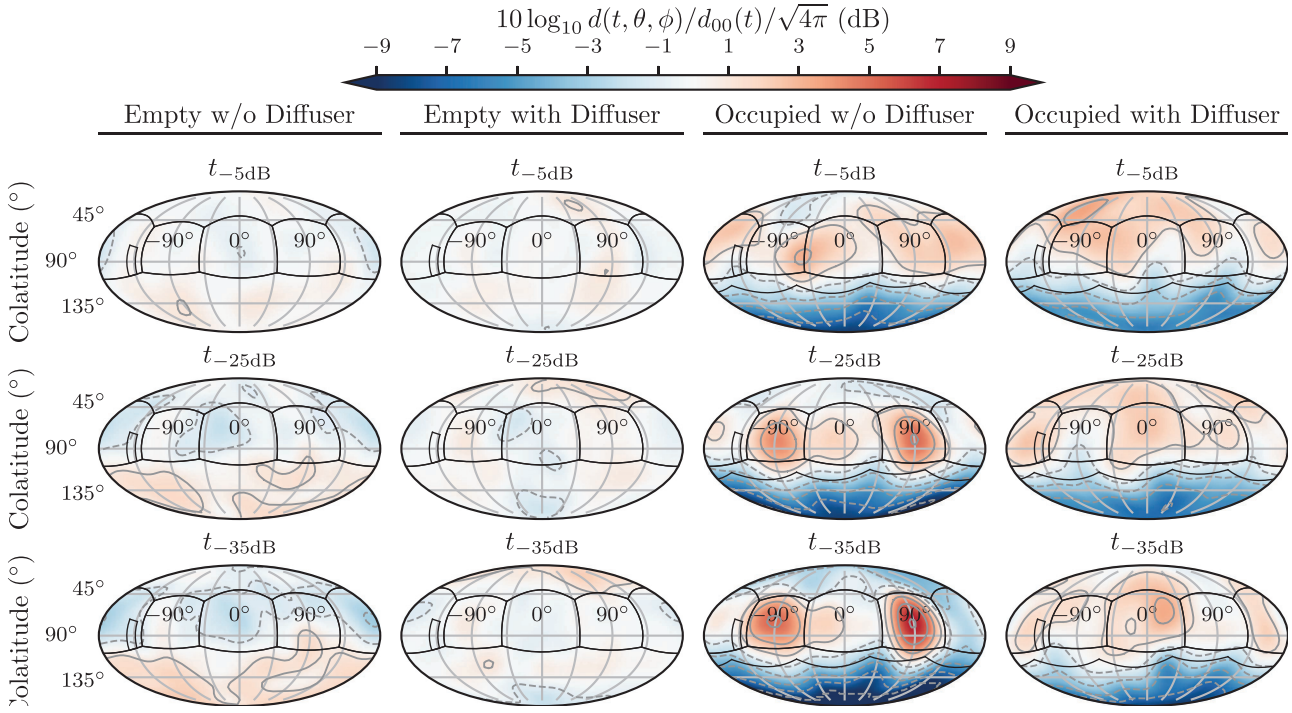

FIG. 4. The DEDC normalized by the monopole moment of the SH-DEDC at position R_1 for the 315 Hz third-octave frequency band. Black lines indicate the outline of the room and absorber placement as given in Fig. 2. Gray contour lines mark levels corresponding to the tick labels in the color bar, and dashed lines indicate negative contour levels.

equal to one and are normalized by their respective monopole moment.

Considering the configurations without the absorbing specimen (see the first two columns of Fig. 5), the energy is primarily contained in SH orders up to three, more specifically in the respective zero degree coefficients, which reflect rotational symmetry with respect to the z axis (Jammalamadaka and Terdik, 2019). Evidently, the energy contained in the first, second, and third order harmonics increases during the decay process for both configurations. This is most prominent if no panel diffusers are installed. Note that the energy contained in the dipole moment $Y_1^0(\mathbf{\Omega})$ for the configuration without panel diffusers is caused by maxima in incident energy previously observed in the lower hemisphere in the first column of Fig. 4.

If the absorbing specimen is present, a general increase in energy contained in higher order harmonics up to order six is observed; see the right two columns of Fig. 5. Again, the energy contained in orders above one increases with progressing energy decay, which is most prominent if no panel diffusers are mounted. Especially, second and fourth order harmonics with large energy levels are observed. These harmonics reflect the maxima at $\theta = 90°$ and $\phi = [\pm 90°, 0°, 180°]$, i.e., in directions corresponding to positive and negative x and y axes, in the energy distributions observed in the

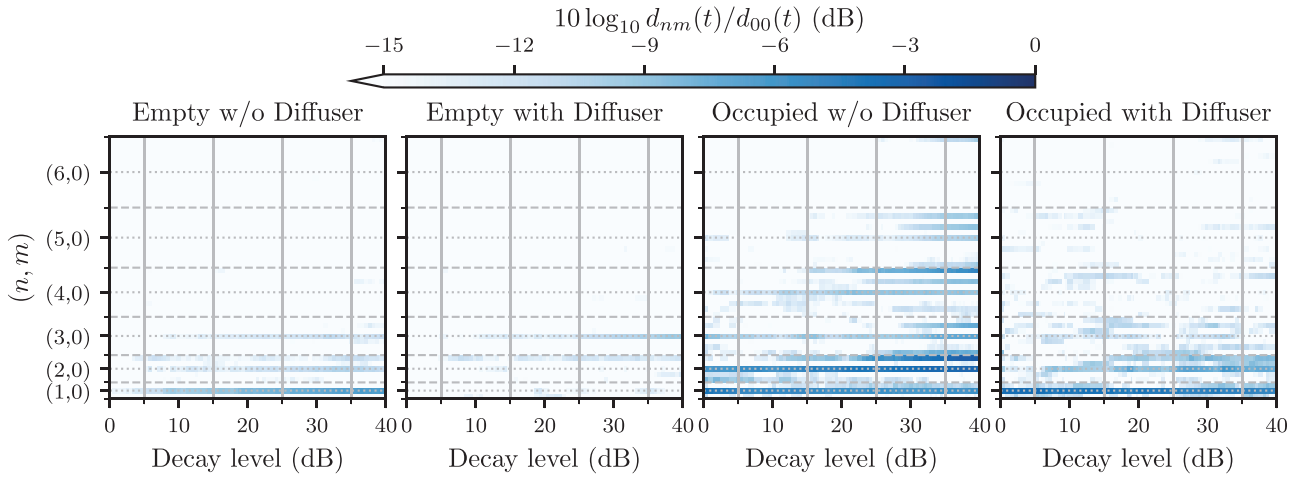

FIG. 5. The SH-DEDCs normalized by the monopole moment at position R_1 for the 315 Hz third-octave frequency band. Dashed horizontal lines separate the SH orders, and dotted lines indicate zeroth degree coefficients.

https://doi.org/10.1121/10.0039531

third column of Fig. 4. Note that the quadrupole moment $Y_2^2(\boldsymbol{\Omega})$, which is aligned with the x and y axes is especially prominent (see also Fig. 1).

The reduced energy variations previously observed in Fig. 4 when panel diffusers are mounted in the laboratory are also well reflected in the SH-DEDC. A reduction in energy levels above SH orders of two is found when comparing the occupied configurations with and without panel diffusers in Fig. 5. Nevertheless, the axial symmetry with respect to the x axis is still evident, as well as a temporal energy increase in second order harmonics.

3. Spatio-spectral dependency of angular distributions

Compared to the differences between room configurations, the differences in the DEDC across receiver positions are only marginal for both empty room configurations. The angular energy patterns resulting from axial and tangential modes previously observed in Fig. 4 are found to be qualitatively consistent across all receiver positions. For the occupied configuration without panel diffusers, distinct maxima with temporally increasing magnitude are observed for all frequency bands. In contrast, such distinct maxima are no longer observed for frequency bands above 500 Hz in the occupied configuration, including panel diffusers, indicating that the panel diffusers effectively scatter the sound field and reduce the prominence of axial and tangential modes. Similarly, no distinct maxima are observed for both empty room configurations for frequency bands above 500 Hz.

In the occupied configurations, the direction and angular width of the minimum in incident energy depends on the placement of the receiver relative to the absorbing specimen. For all frequency bands, a reduction in magnitude and width is observed for position R_3 compared to positions R_1 and R_2 as a result of the increased distance from the absorbing specimen.

Additional figures of the DEDCs and SH-DEDC for all receiver positions and frequency bands are provided as supplementary material in Berzborn *et al.* (2025a).

B. Symmetry based reconstruction

Figure 6 shows the original and reconstructed DEDCs captured at R_1 without (top row) and with (bottom row) panel diffusers for the 1250 Hz frequency band. The reconstructed DEDCs constitute axially symmetric and non-axially symmetric components. The monopole moment is included in both reconstructions; cf. Sec. III C.

If no panel diffusers are mounted, the energy incident during the sound field decay is dominated by a small number of modes with directions of propagation parallel to the absorbing specimen. These maxima correspond to slowly decaying axial modes in the x and y axes and are captured well in the reconstructed DEDC; see top center graph in Fig. 6. In contrast, the reconstruction using the residual harmonics shows a distinct rotational symmetry with respect to the z axis. More specifically, an almost uniform distribution of incident energy in the upper hemisphere and respective uniform distribution of reduced incident energy in the lower hemisphere are observed. This indicates an almost uniform energy incident onto the absorbing specimen centered below the receiver and outlined in black.

The axial symmetry is primarily reflected in the second and fourth order harmonics with respective levels of up to −3 dB and −6 dB below the monopole moment; see the SH-DEDC in Fig. 22 in the supplementary material (Berzborn *et al.*, 2025a). Interestingly, the energy distributions up to second order are almost constant during the entire decay process, whereas energy contributions in higher

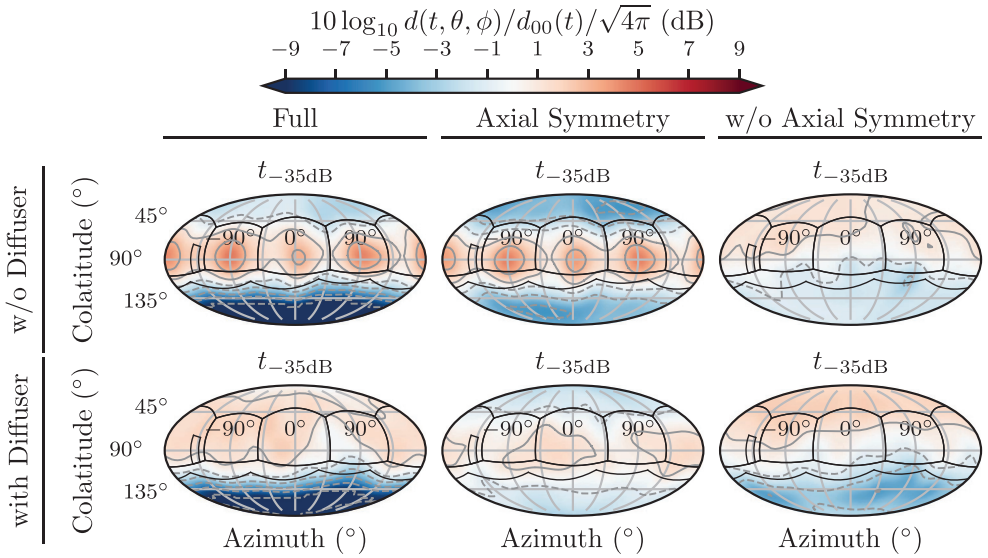

FIG. 6. Original and partially reconstructed DEDCs captured at R_1 without (top row) and with (bottom row) panel diffusers for the 1250 Hz frequency band. Black lines indicate the outline of the room and absorber placement as given in Fig. 2. Grey contour lines mark levels corresponding to the tick labels in the color bar.

orders start to increase for omnidirectioal energy decay levels below −15 dB.

In comparison to the configuration without panel diffusers mounted, the distribution of incident energy is more uniform in the original DEDC: no distinct maxima are found and angular variations are below 3 dB in the upper hemisphere as evident in the bottom left of Fig. 6. This indicates an almost uniform flow of energy into the absorbing specimen. Interestingly, a similar distribution of incident energy is observed when comparing the non-axially symmetric DEDC reconstructions for the room with and without panel diffusers; see center column of Fig. 6, which is not immediately discernible from the original DEDC. No significant temporal trends are observed during the decay, indicating a uniform damping of the modes constituting the sound field.

Similar temporal effects and energy distributions are observed for all frequency bands above 500 Hz if the absorbing specimen is present in the room. At receiver position R_3, a concentration of energy in the $Y_1^0(\boldsymbol{\Omega})$ dipole harmonic is not observed as a result of lacking symmetry with respect to the placement of the receiver relative to the absorber. The similarity of the residual reconstructions between the two configurations, including the absorbing specimen, however, remains similar to the observations made at receiver position R_1 and R_2. See Figs. 25–27 of the supplementary material (Berzborn *et al.*, 2025a).

C. Symmetry quantification

In the following, all graphs are given as a function of decay level instead of time, allowing for a more consistent comparison independent of the individual reverberation times of respective configurations. The results in Secs. V C 1, V C 2, and V C 4 are presented as spatial averages across the three receiver positions. This representation is suitable because the temporal evolution of the isotropy estimator is found to be primarily influenced by the room configuration and frequency band while differences with respect to receiver positions are small. The standard deviation across receiver positions is discussed separately in Sec. V C 3.

1. Full spherical symmetry

Figure 7 shows the mean and standard deviation, calculated across all receiver positions, of the estimated isotropy for the 315 Hz, 500 Hz, 800 Hz, and 1.25 kHz frequency bands. At 315 Hz, it is apparent that the estimated isotropy is strongly dependent on the decay level in the analyzed frequency band. For both configurations without the test specimen, the maximum average isotropy with a value of 0.65 is observed in steady state. The average isotropy decreases during the decay process to 0.5 if no panel diffusers are mounted and 0.4 with mounted panel diffusers. The rate at which the isotropy decreases is higher for the configuration without panel diffusers. This decrease is first a result of the increase in near-field effects and, second, because of the de-mixing of the sound field caused by the tangential modes decaying at a slower rate; cf. Sec. V A.

For the configurations including the test specimen, the estimated isotropy is reduced, which is primarily caused by the distinct flow of energy toward the absorbing specimen as previously observed in Fig. 4. In contrast to the configurations without the test specimen, the isotropy evolution is not monotonously decreasing. It is an approximately linear function with a piecewise constant gradient, initially increasing because of the density of early distinct-direction reflections, then plateauing and decreasing during the late part of the decay process. The aforementioned initial increase is typically compressed on the decay level scale as the EDC shows discrete steps of energy drops. The onset of the decrease is linked to the de-mixing of the sound field observed. In the case of the configuration without panel diffusers, the inflection point is found earlier at a decay level proportional to −20 dB, and the gradient is steeper. The variations with respect to receiver positions are similar to the observations for the configurations without the test

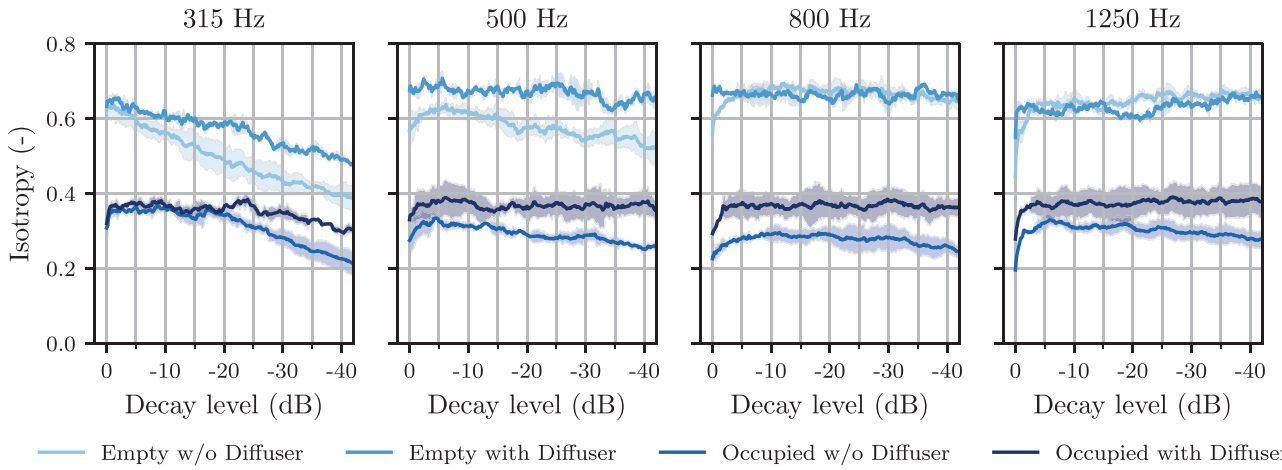

FIG. 7. Spatial mean and standard deviation of the estimated isotropy. The decay level (x axis) is proportional to the omnidirectional decay function. A higher value indicates a more isotropic sound field.

https://doi.org/10.1121/10.0039531

specimen, that is, the temporal evolution of the isotropy estimator are similar for all receiver positions.

The temporal decrease observed for the 315 Hz frequency band is less pronounced or not observed in higher frequency bands. Nevertheless, most frequency bands—especially in room configurations not including panel diffusers—show an initial increase in isotropy within the first 5 dB followed by subsequent decrease. The largest differences in the isotropy slope are observed for the configurations without the test specimen, where the magnitude of the gradient decreases with increasing frequency. In both configurations, this is found to be a result of nonuniform modal damping, as observed in Fig. 4. Especially in the 500 Hz frequency band, axial modes in the z axis decaying at a slower rate are found. Additional DEDCs visualizations have been omitted for brevity.

In contrast, the absolute change in the gradient of the estimated isotropy is smaller for the configurations that include the test specimen. Yet, again, if no panel diffusers are mounted, the isotropy function does not converge to a constant level for any of the frequency bands. Similar to before, this is linked to tangential and, even more so, axial modes propagating parallel to the absorbing specimen and decaying at a lower rated compared to modes with oblique incidence on the specimen, as observed in Figs. 4 and 6.

Interestingly, the quantitative differences within the first 20 dB of the decay process indicate the highest isotropy value for the 315 Hz frequency band, which at first seems counterintuitive because of typically lower modal density and, hence, lower number of waves constituting the sound field at low frequencies. However, comparing the incident energy distributions in Figs. 4 and 6, it is evident that during the early part (cf. $t_{-5\mathrm{dB}}$) of the decay that the energy distribution is indeed more uniform in the 315 Hz frequency band. This primarily seems to be caused by a much earlier de-mixing of the sound field for frequency bands above 500 Hz. As observed in Fig. 7, with panel diffusers in the room, the isotropy function converges to approximately 0.35 for frequency bands above 500 Hz. Figure 7 also shows that the overall isotropy is increased for all frequency bands if panel diffusers are employed, which is to be expected as a result of the increased diffusion of the sound field.

2. Axial symmetry

The spatial average of the estimated axial symmetry is depicted in Fig. 8. It should be highlighted once more that in contrast to the full spherical symmetry, a lower value in the axial symmetry estimate indicates a more isotropic sound field. Most notably, the axial symmetry shows a prominent temporal increase for the occupied room without panel diffusers. The increase is most notable in the 315 Hz frequency band, and it is also observed for all other configurations, albeit with smaller gradients. The increase in axial symmetry resulting from incident energy caused by axial and tangential modes observed for the DEDC at position R_1 (see Fig. 4) is well reflected. In contrast to the estimated isotropy, the axial symmetry evolution does not show plateaus for the room configuration without panel diffusers but is nearly linearly increasing. These results indicate that the decrease in estimated sound field isotropy during the decay process is primarily caused by an increase in axial symmetry, which is in line with observations made in Sec. V A.

For the room configuration with test sample and panel diffusers installed, the axial symmetry is approximately constant until a decay level of −25 dB and then increases, which coincides with the change in gradient found in the estimated isotropy in Fig. 7. For frequency bands above 315 Hz, the axial symmetry estimates remain constant and equal for all frequency bands if panel diffusers are installed. This indicates that the quantitative differences between frequency bands are not caused by axial symmetries. Despite the more distinct temporal evolution of axial symmetry compared to isotropy, the quantitative differences across frequency bands diminish for most of the decay process in the configuration without panel diffusers or are unnoticeable with them.

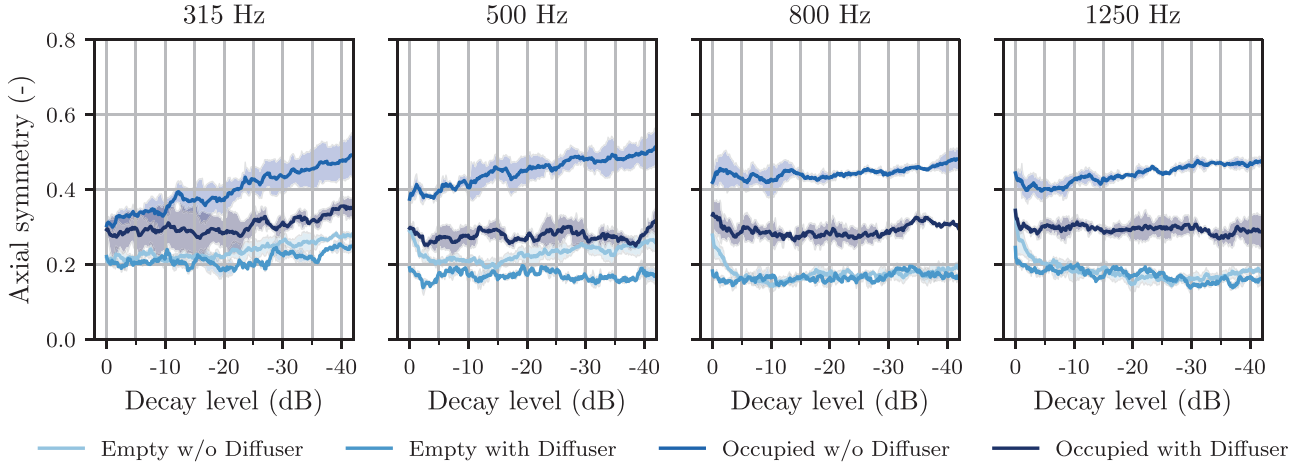

FIG. 8. Spatial mean and standard deviation of the estimated axial symmetry. The decay level (x axis) is proportional to the omni-directional decay function. A lower value in the axial symmetry estimate indicates a more isotropic sound field.

Considering both empty configurations, the increase in axial symmetry is less pronounced when compared to the decrease in estimated isotropy in Fig. 7: a maximal increase of 0.1 is observed when no panel diffusers are mounted. Again, this agrees with previously made observations depicted in Fig. 4, in which only a slight increase in axial symmetry in the incident energy caused by tangential modes in the *yz*-plane is found. For frequency bands above 500 Hz, the estimated axial symmetry is approximately constant below decay levels of −5 dB.

3. Spatial dependency of the estimators

As previously stated, the overall temporal evolution of the isotropy estimators does not significantly depend on the receiver position but is found to be primarily influenced by the room configuration and frequency band. Quantitative differences in both estimators with respect to receiver positions largely depend on the frequency band and room configuration and the value of the estimator itself. Especially in cases where the estimated isotropy value is large, the differences between receiver positions are small, hence, resulting in a small spatial standard deviation; see estimates for the empty room for frequency bands of 500 Hz and above in Fig. 7. This is plausible, as an isotropic sound field is expected also to be homogeneous with respect to the receiver positions. Similarly, small inter-receiver differences in the isotropy estimate are found when energy distributions corresponding to distinct mode groups are observed, such as in room configurations omitting panel diffusers and at low frequencies. In such cases, the underlying energy distributions are found to be largely independent from receiver position regardless of the position with respect to the absorbing specimen. The largest spatial standard deviation for the estimated isotropy is found in the occupied room with panel diffusers for frequency bands of 500 Hz and above. This increase is a result of an increase in sound field isotropy by up to 0.1 for receiver R_3, which is positioned next to the absorbing specimen (additional figure omitted for brevity). This reflects the smoother energy distribution found in the respective DEDCs, primarily caused by a decreased influence of the absorbing specimen, that is, local incident energy minima in the direction of the absorbing sample are less pronounced; see Figs. 4–6 of the supplementary material (Berzborn *et al.*, 2025a)

Similar to the observations made for the isotropy estimator, the spatial standard deviation of the axial symmetry is found to be almost zero if the sound field is isotropic. Additionally, the spatial standard deviation of the axial symmetry estimator is typically found to be lower compared to the isotropy estimator. Overall, the standard deviation decreases with increasing frequency for most configurations. The large standard deviation (up to 0.15) at low frequencies is primarily a result of diffraction of normal and tangential modes in the *xy*-plane caused by the absorbing specimen, as well as a distinct influence of axial modes in the *z* axis at receiver position R_3.

4. Correlation with instantaneous decay rate

Figure 9 shows the instantaneous decay rate as a function of energy level extracted from the omnidirectional EDC, which are both averaged over the three receiver positions. Note that the initial 5 dB are omitted because of artifacts attributed to the discontinuity of the EDC for $t < 0$. Similar smoothing artifacts are found at the end of the EDC but are less pronounced; these are visible in the 315 Hz for the empty room configurations for decay levels below −30 dB. It is most prominent that despite application of a smoothing filter with a window length of $T_{20}/12$, the instantaneous damping is not a smooth function but—especially for all configurations including the absorbing specimen—exhibits significant fluctuations. The comparably larger fluctuations found for configurations including the absorbing sample are caused by shorter decay times (Davy, 1989) and nonuniform distribution of absorption. Note that the instantaneous temporal fluctuations relative to the decay

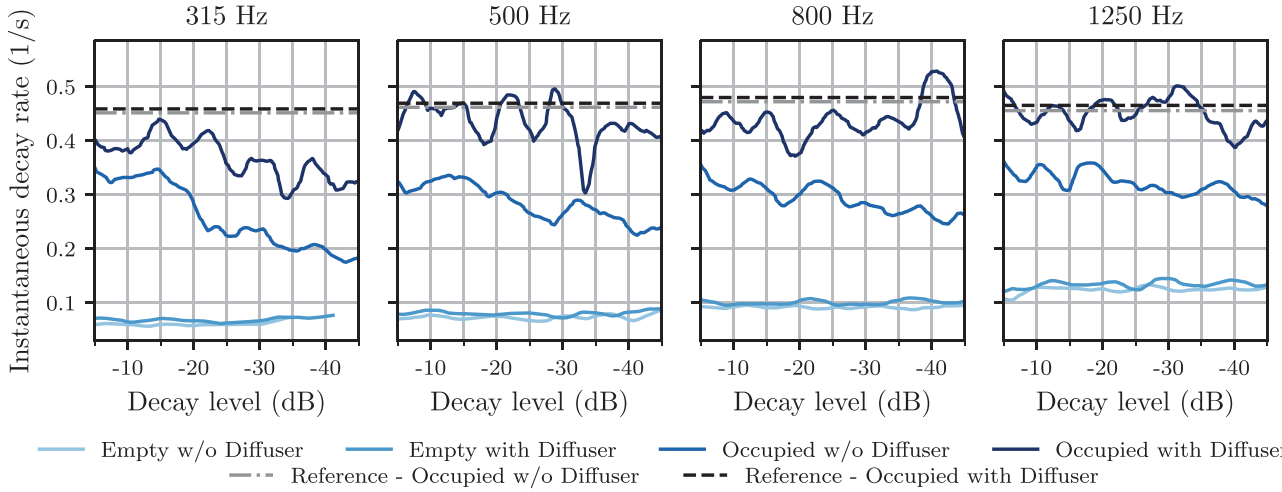

FIG. 9. Instantaneous decay rate of the omnidirectional EDC averaged over the three receiver positions. Reference values are calculated based on Eyring's equation using the reverberation time T_{60} of the empty room given in Fig. 3 and the reference finite-size random incidence absorption coefficient from Table I.

https://doi.org/10.1121/10.0039531

rate—that is, the instantaneous damping multiplied by the respective reverberation time—are comparable.

Nevertheless, a general temporal trend is observed: the instantaneous damping decreases during the decay process for all frequency bands when the absorbing sample is placed in the room and no panel diffusers are mounted. The same trend is observed for the 315 Hz frequency band when panel diffusers are mounted. This indicates that the decay process clearly is multi-exponential, and significant curvature of the respective EDC is observed. This phenomenon is quite well discussed in the literature and primarily attributed to the nonuniform distribution of absorption in the room (Kuttruff, 1958; Hunt *et al.*, 1939). It typically results in an underestimation of the reverberation time when estimated using linear regression from the respective T_{20} or T_{30} intervals as observed in Fig. 3. Note that a slight decrease in damping is also observed for the 500 Hz band, which is more noticeable when comparing the reciprocal differences in the values for T_{20} and T_{60} in Fig. 3. In contrast, the instantaneous damping is approximately constant and proportional to the reciprocal of the reverberation times reported in Fig. 3. The same is observed for the occupied room, including panel diffusers for frequency bands above 500 Hz.

For reference, Fig. 9 also shows the predicted decay rates for configurations including the absorbing specimen. These are calculated using the Eyring (1930) equation. The absorption coefficients of the empty room configurations are calibrated using the reverberation times T_{60} from Fig. 3, assuming that these are sufficiently accurate. It is most apparent that in all occupied configurations where the symmetry estimators are not constant during the decay process, additionally, the instantaneous decay rate is found to be lower than the expected theoretical values.

Comparing Fig. 9 with Fig. 7 indicates a high correlation between the temporal evolution of instantaneous damping and isotropy. This is quantified using the normalized cross-correlation function at zero temporal overlap, which yields values of almost one when calculated for the spatially averaged isotropy and instantaneous damping functions; cf. Table II. Note that the correlation coefficients for the empty room most probably are overestimated here because the instantaneous damping function is truncated at a decay level of approximately −25 dB. Again, this is most probably a result of model mismatches, such as near-field effects or evanescent waves, during decomposition of the sound field.

Such high correlation values are plausible as the decomposition of the sound field does not affect the temporal behavior of the sound field but constitutes only a magnitude weighting. As a consequence, the symmetry estimators are magnitude-weighted ratios of decaying exponential decay functions. Interestingly, the instantaneous damping of the omnidirectional EDC results in a similar ratio when assuming that the sound field is described as a sum of decaying exponential functions; see Appendix B.

TABLE II. Cross correlation between the spatially averaged isotropy and instantaneous decay rate at zero temporal overlap.

	315 Hz	500 Hz	800 Hz	1.25 Hz
Empty without diffusers	0.987	0.994	0.991	0.994
Empty with diffusers	0.996	0.998	0.996	0.996
Occupied without diffusers	0.998	0.997	0.991	0.996
Occupied with diffusers	0.998	0.999	0.997	0.997

VI. GENERAL DISCUSSION

The validity of the present analysis method is primarily constrained by the measurement system. Spatial aliasing is expected to significantly alter the results for frequencies above 3 kHz. Additionally, influences resulting from scattering at the robotic arm start to appear above 2 kHz. Hence, yielding an upper bound of 2 kHz. Loss of signal quality caused by amplification of sensor noise and model mismatches imposes a lower limit of approximately 200 Hz. Additionally, for very low frequencies, where the modal density is drastically reduced, a grouping of modes is no longer feasible as the eigenfrequencies and directions of radiation of waves becomes sparse. In this case, approaches based on Mignot *et al.* (2014) or Pham Vu and Lissek (2020) would be more suitable.

Although the effect of frequency bandwidth of fractional octave filters on the DEDC is equal to its omnidirectional counterpart, it does not affect the symmetry estimation, which is only performed with respect to directions. Nevertheless, a temporal smoothing of the initial decay occurs if very narrow band filters are used.

Importantly, the definition of the DEDC based on the two-dimensional wave number spectrum does not allow for a strict separation of individual decaying modes but rather a separation into groups of plane waves representing modes with shared directions of radiation. Accordingly, the two-dimensional wave number spectrum is assumed to represent a projection of the three-dimensional wave number lattice found in the works of Hunt *et al.* (1939). To achieve adequate angular separation of incident energy in the presence of multiple modes per frequency band, the sidelobes need to be suppressed as best as possible while maintaining a narrow mainlobe. This is crucial as an insufficient separation in incident waves results in interference effects and, consequently, distortions in the estimated DEDCs. As a result, their temporal behavior is not necessarily identical and the decay function of these directions may be distinctly multi-exponential. The Dolph-Chebyshev beamformer employed here is found to achieve an adequately narrow mainlobe and sufficient sidelobe attenuation for a wide frequency range. It further ensures a constant angular mainlobe resolution, which is crucial for consistent estimates of isotropy and axial symmetry.

VII. IMPLICATIONS CONCERNING ISO 354:2003

The present results highlight the occurrence of distinctly anisotropic energy distributions in the studied reverberation room, most prominently when an absorbing sample is mounted in the room. Especially the temporal increase in

anisotropy resulting from increased axial symmetry can be linked to a separation of the sound field decay into slowly decaying waves propagating parallel to the absorbing sample and waves with grazing incidence. As evident from Sec. V C 4, the temporal evolution of the isotropy estimator and instantaneous decay rate of the omnidirectional EDC are correlated.

The correlation between the estimator and instantaneous decay rate does, however, not imply that the decay rate or EDC slope are suitable isotropy indicators. Isotropic sound fields may also exhibit nonconstant instantaneous decay rate, especially when spatially uniform boundary conditions vary significantly within a frequency band. The instantaneous decay rate, if not a constant, may only serve as an indicator for potential reverberation time regression errors when assuming a single-exponential decay. Also, note that it is not suited to infer a physically meaningful decay time as the function may take any value between the maximum and minimum modal damping of the sound field; see also Eq. (B3).

Yet, the temporal evolution in isotropy or axial asymmetry results from the distinct de-mixing with respect to the angular distributions of incident energy and the damping of mode groups with respect to time (see Figs. 4–6). Accordingly, the temporal evolution of symmetry estimators not only signifies anisotropy in incident energy distribution but may also relate to temporal regression errors from sound field de-mixing caused by uneven mode damping. This indicates that a nonconstant isotropy and axial symmetry estimator function may additionally hint at regression errors in the estimation of reverberation times as observed in Fig. 3. However, it is important to note that the evolution of the isotropy estimator is not generally suited to identify valid reverberation time regression ranges, which was suggested by Nolan *et al.* (2020) for the following reasons. First, from Fig. 8, it is obvious that in the present results, the increasing anisotropy is a result of an increase in axial symmetry (see also Figs. 4 and 5), occurring much earlier than the inflection point of the isotropy estimator. Second, the instantaneous decay rate (see Fig. 9) is not constant within decay ranges with maximal isotropy. As a result, even when a state of maximal isotropy is reached, regression errors in the reverberation time estimation are still to be expected. This is most evident when comparing the estimated instantaneous decay rate to the expected theoretical values in Fig. 9. In such cases, a full identification of the multi-exponential decay process as presented by Balint *et al.* (2019) is required to achieve a physically meaningful characterization of the decay process. The identification may even be extended to consider damping distributions with respect to the direction of incidence, as presented by Berzborn *et al.* (2021), Berzborn and Vorländer (2025), and Götz *et al.* (2023).

VIII. CONCLUSIONS

The present experimental study investigates the directional properties of sound fields in a reverberation room during the decay process. The analysis method is based on the measurement of DEDCs, which are calculated from a plane wave decomposition of the sound field. The sound field decomposition is based on the decomposition of the microphone array signals into SH, enabling an elegant framework for the generation of robust spatial filter functions with equal angular resolution and good signal-to-noise ratio over the entire frequency range. This allows for a spatiotemporal analysis of the incident energy at a high temporal resolution. Based on the SH-DEDCs, estimators for the full spherical symmetry as well as axial symmetry of energy distributions are applied. Especially the high signal-to-noise ratio is beneficial because it allows for the analysis of sound field decay beyond levels of −45 dB. This is most important in sound fields with highly anisotropic decay rates as directions decaying very quickly into the noise floor limit the range for which the estimators can be applied.

Results obtained in a rectangular reverberation in different configurations—with and without an absorbing sample, where both are under application of panel diffusers and without—showed anisotropy of the sound field for configurations including the absorbing sample, which were more pronounced when no panel diffusers were employed. However, especially in low and mid frequency bands, the analysis revealed frequency bands in which the panel diffusers do not have a significant effect in increasing the diffusion of the sound field. A temporal increase in anisotropy in the incident energy distribution was found for all frequency bands if the absorbing sample was mounted inside the room if panel diffusers were removed, and for the 315 Hz frequency band if panel diffusers were mounted. This temporal increase in anisotropy was found to be caused by the multi-exponential energy decay comprised of weakly damped axial modes and strongly damped modes with grazing incidence on the absorbing sample and is in line with the theory of modal energy decay developed by Hunt *et al.* (1939). However, further analysis of the directional damping properties is beyond the scope of this work. The interested reader is referred to Berzborn *et al.* (2021) and Berzborn and Vorländer (2025). These effects were well reflected in the temporal decrease in the estimated isotropy and the increase in estimated axial symmetry. For room configurations, where the use of panel diffusers evidently increased the diffusion of the sound field, an increased dependence on the receiver position was observed. The study conclusively demonstrates a strong correlation between the decrease in the isotropy estimator and the temporally variable instantaneous decay rate. However, it is important to note that the isotropy estimator's temporal evolution is not a reliable method for deriving new reverberation time regression intervals to circumvent systematic errors.

It is expected that the information about the energy distribution, with respect to direction and time and provided by the method, is a valuable tool for future investigations on the poor interlaboratory reproducibility known to exist in the determination of Sabine's absorption coefficient. Respective future research using the method should involve

https://doi.org/10.1121/10.0039531

a larger variety of different laboratories and their configurations with respect to diffusing elements. Additional research on the relationship between the results from the presented method and the respective absorption coefficient error should, however, be prioritized before conducting extensive interlaboratory measurements.

ACKNOWLEDGMENTS

The present work was supported by the German Research Foundation (DFG) under Grant No. 298797807. The authors would like to thank Samuel A. Verburg for his assistance in setting up the experiments, as well as Jamilla Balint for many fruitful discussions and proofreading the manuscript.

AUTHOR DECLARATIONS

Conflict of Interest

The authors have no conflicts to disclose.

DATA AVAILABILITY

The data that support the findings of this study are openly available in Berzborn *et al.* (2025b). Additional figures are available in Berzborn *et al.* (2025a).

APPENDIX A: NUMERIC RANDOM INCIDENCE ABSORPTION COEFFICIENT

The reference finite-size random incidence absorption coefficient was calculated using the finite-element method (FEM)/boundary-element method (BEM) coupling implemented in *Comsol-Multiphysics version 6.3*, similar to the approach proposed by Pereira *et al.* (2021). Instead of using a synthesized diffuse sound field, the absorbed power is simulated for single plane wave incidence from directions Ω and subsequently averaged. The glass wool is modelled as a transversely isotropic equivalent fluid based on the Johnson-Champoux-Allard (JCA) model (Allard and Atalla, 2009). The pore parameters were identified from impedance tube measurements using stochastic model inversion. The approach is detailed in Berzborn and Vorländer (2024). The JCA model parameters used in this work are given in Table III. Cavalieri *et al.* (2025) reported similar pore parameters for the Johnson-Champoux-Allard-Lafarge model.

The random incidence absorbed power is calculated by integrating over the sphere, denoted by Ω, for a sufficient number of incident plane waves,

$$\tilde{P}_{\mathrm{abs}}(k) = \int_{\Omega} P_{\mathrm{abs}}(k,\Omega)\,\mathrm{d}\Omega = \int_{\Omega}\int_{S} \mathbf{I}\cdot\mathbf{n}\,\mathrm{d}S\,\mathrm{d}\Omega, \tag{A1}$$

where $\mathbf{I}$ is the real part of the intensity vector on the surface of the absorber, and $\mathbf{n}$ is the respective normal vector of the surface element S. In this work, an angular resolution of 5° was used. The power of the incident plane wave is calculated analogously to Thomasson (1980). Note that only normal intensity components on the top surface have a nonvanishing contribution to the incident power. The finite-size random incidence absorption coefficient is finally calculated as the ratio $\tilde{\alpha} = \tilde{P}_{\mathrm{abs}}(k)/\tilde{P}_{\mathrm{inc}}(k)$.

TABLE III. JCA parameters of the absorbing specimen. ϵ is the porosity, α_∞ is the tortuosity, Λ' is the thermal characteristic length, and $\sigma^{(T/I)}$ and $\Lambda^{(T/I)}$ are the flow resistivity and viscous characteristic lengths for the transverse and isotropic directions, respectively.

ϵ	α_∞	$\sigma^{(T)}$	$\sigma^{(I)}$	$\Lambda^{(T)}$	$\Lambda^{(I)}$	Λ'
(−)	(−)	$\left(\frac{\mathrm{Pa\,s}}{\mathrm{m}^2}\right)$	$\left(\frac{\mathrm{Pa\,s}}{\mathrm{m}^2}\right)$	(μm)	(μm)	(μm)
0.997	1.06	5208	9137	92	149	168

APPENDIX B: DECAY RATE AND ISOTROPY EVOLUTION DURING MULTI-EXPONENTIAL DECAY

Assuming that the EDC is a superposition of $i \in [1, I]$ exponential decays with energy a_i and damping constant δ_i written as (Kuttruff, 1958)

$$e(t) = \sum_{i=1}^{I} a_i e^{-\delta_i t}, \tag{B1}$$

the decay rate [cf. Eq. (7)] can be written as

$$\gamma(t) = -C\frac{\sum_{i=1}^{I} a_i\delta_i e^{-\delta_i t}}{\sum_{i=1}^{I} a_i e^{-\delta_i t}}, \tag{B2}$$

where $1/C = 60\,\ln(10)/10 \approx 13.8$. On the other hand, assuming that the omnidirectional EDC and the monopole moment of the DEDC are proportional, the isotropy estimator defined in Eq. (9) is proportional to

$$\iota_\Omega(t) \propto \frac{\sum_{i=1}^{I} a_i e^{-\delta_i t}}{\sum_{i=1}^{I} a_i e^{-\delta_i t} + \sum_{n=1}^{\tilde{N}}\sum_{m=-n}^{n} |d_{nm}(t)|}. \tag{B3}$$

Because the SH transform and prior plane wave decomposition are linear magnitude weightings, the SH-DEDC is expected to be proportional to a re-weighted version of Eq. (B1). Hence, Eqs. (B2) and (B3) only differ in the multiplication with δ_i in the numerator of Eq. (B2) and the addition of the magnitude sum of SH-DEDC moments above one. The latter is generally not negligible when compared to $e(t)$ as their ratio depends on the isotropy of the sound field.

Allard, J.-F., and Atalla, N. (**2009**). *Propagation of Sound in Porous Media: Modelling Sound Absorbing Materials*, 2nd ed. (Wiley, Hoboken, NJ).
Balint, J., Berzborn, M., Nolan, M., and Vorländer, M. (**2023**). "Measuring sound absorption: The hundred-year debate on the reverberation chamber method," Acoust. Today **19**(3), 13–20.
Balint, J., Muralter, F., Nolan, M., and Jeong, C.-H. (**2019**). "Bayesian decay time estimation in a reverberation chamber for absorption measurements," J. Acoust. Soc. Am. **146**(3), 1641–1649.

Berzborn, M., Balint, J., and Vorländer, M. (**2021**). "On the estimation of directional decay times in reverberation rooms," in *Proceedings of Euronoise*, Madeira, Portugal (October 25–27, 2021) (Portuguese Acoustical Society, Lisboa, Portugal), pp. 1515–1523.
Berzborn, M., Bomhardt, R., Klein, J., Richter, J.-G., and Vorländer, M. (**2017**). "The ITA-Toolbox: An open source MATLAB Toolbox for acoustic measurements and signal processing," in *Proceedings of the 43rd Annual German Congress on Acoustics*, Kiel, Germany (March 6–9, 2017) [German Acoustical Society (DEGA), Berlin, Germany], pp. 222–225.
Berzborn, M., Nolan, M., Fernandez Grande, E., and Vorländer, M. (**2025a**). Supplementary material to: Directional sound field decay analysis in a reverberation room (0.1.0) [Data set]. Zenodo. https://10.5281/zenodo.17650326
Berzborn, M., Nolan, M., Fernandez Grande, E., and Vorländer, M. (**2025b**). "Directional room impulse responses measured in reverberation rooms" [data set]. Zenodo. https://10.5281/zenodo.17857243
Berzborn, M., and Vorländer, M. (**2021**). "Directional sound field decay analysis in performance spaces," Build. Acoust. **28**(3), 249–263.
Berzborn, M., and Vorländer, M. (**2024**). "Inference of the acoustic properties of transversely isotropic porous materials," in *Proceedings Of Internoise*, Nantes, France (August 25–29, 2024) (International Institute of Noise Control Engineering, Luzern, Switzerland), pp. 8339–8344.
Berzborn, M., and Vorländer, M. (**2025**). "Stochastic variational inference of directional decay times in a reverberation room," in *11th Convention of the European Acoustics Association, Forum Acusticum/Euronoise 2025*, Malaga, Spain (June 23–26, 2025) (Spanish Acoustics Society, Madrid, Spain), pp. 1–6.
Cavalieri, T., Nolan, M., Gaborit, M., and Groby, J.-P. (**2025**). "Experimental characterization of fully-anisotropic equivalent fluids from normal incidence measurements," J. Sound Vib. **608**, 119051.
Chardon, G., Kreuzer, W., and Noisternig, M. (**2015**). "Design of spatial microphone arrays for sound field interpolation," IEEE J. Sel. Top. Signal Process. **9**(5), 780–790.
Davy, J. (**1989**). "The variance of the curvature of reverberant decays," J. Sound Vib. **128**(2), 297–305.
Epain, N., and Jin, C. T. (**2016**). "Spherical harmonic signal covariance and sound field diffuseness," IEEE/ACM Trans. Audio. Speech. Lang. Process. **24**(10), 1796–1807.
Eyring, C. F. (**1930**). "Reverberation time in dead rooms," J. Acoust. Soc. Am. **1**, 217–240.
García-Portugués, E., and Verdebout, T. (**2018**). "An overview of uniformity tests on the hypersphere," arXiv:1804.00286.
Götz, G., Schlecht, S. J., and Pulkki, V. (**2023**). "Common-slope modeling of late reverberation," IEEE/ACM Trans. Audio. Speech. Lang. Process. **31**, 3945–3957.
Gover, B. N., Ryan, J. G., and Stinson, M. R. (**2002**). "Microphone array measurement system for analysis of directional and spatial variations of sound fields," J. Acoust. Soc. Am. **112**(5), 1980–1991.
Gover, B. N., Ryan, J. G., and Stinson, M. R. (**2004**). "Measurements of directional properties of reverberant sound fields in rooms using a spherical microphone array," J. Acoust. Soc. Am. **116**(4), 2138–2148.
Guski, M., and Vorländer, M. (**2014**). "Comparison of noise compensation methods for room acoustic impulse response evaluations," Acta Acust. Acust. **100**(2), 320–327.
Halliwell, R. E. (**1983**). "Inter-laboratory variability of sound absorption measurement," J. Acoust. Soc. Am. **73**(3), 880–886.
Herzog, A., and Habets, E. A. (**2021**). "Generalized intensity vector and energy density in the spherical harmonic domain: Theory and applications," J. Acoust. Soc. Am. **150**(1), 294–306.
Hunt, F. V., Beranek, L. L., and Maa, D. Y. (**1939**). "Analysis of sound decay in rectangular rooms," J. Acoust. Soc. Am. **11**(1), 80–94.
ISO 354:2003 (**2003**). "Measurement of sound absorption in a reverberation room" (International Organization for Standardization, Geneva, Switzerland).
Jammalamadaka, S. R., and Terdik, G. H. (**2019**). "Harmonic analysis and distribution-free inference for spherical distributions," J. Multivar. Anal. **171**(5), 436–451.
Kuttruff, H. (**1958**). "Eigenschaften und Auswertung von Nachhallkurven" ("Properties and analysis of energy decay curves"), Acustica **8**(4), 273–280.
Kuttruff, H. (**2009**). *Room Acoustics*, 4th ed. (Taylor and Francis, Milton Park, Oxfordshire, UK).
Leopardi, P. (**2006**). "A partition of the unit sphere into regions of equal area and small diameter," Electron. T. Numer. Anal. **25**(12), 309–327.
Lundeby, A., Vigran, T. E., Bietz, H., and Vorländer, M. (**1995**). "Uncertainties of measurements in room acoustics," Acustica **81**(4), 344–355.
Meyer, E., and Diestel, H.-G. (**1952**). "Hallraumversuche mit gerichteten Sende- und Empfangsanlagen" ("Experiments in reverberation rooms using directional source and receiver apparatus"), Acustica **2**(4), 161–166.
Mignot, R., Chardon, G., and Daudet, L. (**2014**). "Low frequency interpolation of room impulse responses using compressed sensing," IEEE/ACM Trans. Audio Speech Lang. Process. **22**(1), 205–216.
Nolan, M., Berzborn, M., and Fernandez-Grande, E. (**2020**). "Isotropy in decaying reverberant sound fields," J. Acoust. Soc. Am. **148**(2), 1077–1088.
Nolan, M., Fernandez-Grande, E., Brunskog, J., and Jeong, C.-H. (**2018**). "A wavenumber approach to quantifying the isotropy of the sound field in reverberant spaces," J. Acoust. Soc. Am. **143**(4), 2514–2526.
Pereira, M., Mareze, P., Godinho, L., Amado-Mendes, P., and Ramis, J. (**2021**). "Proposal of numerical models to predict the diffuse field sound absorption of finite sized porous materials—BEM and FEM approaches," Appl. Acoust. **180**, 108092.
Pham Vu, T., and Lissek, H. (**2020**). "Low frequency sound field reconstruction in a non-rectangular room using a small number of microphones," Acta Acust. **4**(2), 5.
Politis, A., and Gamper, H. (**2017**). "Comparing modeled and measurement-based spherical harmonic encoding filters for spherical microphone arrays," in *2017 IEEE Workshop on Applications of Signal Processing to Audio and Acoustics*, New Paltz, NY (October 15–18, 2017) (IEEE, New York), pp. 224–228.
Pulkki, V. (**2007**). "Spatial sound reproduction with directional audio coding," J. Audio Eng. Soc. **55**(6), 503–516.
Rafaely, B. (**2015**). *Fundamentals of Spherical Array Processing*, 1st ed., Springer Topics in Signal Processing Vol. 8 (Springer, Berlin, Germany).
Sahoo, I., Guinness, J., and Reich, B. J. (**2019**). "A test for isotropy on a sphere using spherical harmonic functions," Stat. Sinica **29**, 1253–1276.
Savitzky, A., and Golay, M. J. E. (**1964**). "Smoothing and differentiation of data by simplified least squares procedures," Anal. Chem. **36**(8), 1627–1639.
Schroeder, M. R. (**1965**). "New method of measuring reverberation time," J. Acoust. Soc. Am. **37**(6), 1187–1188.
Scrosati, C., Martellotta, F., Pompoli, F., Schiavi, A., Prato, A., D'Orazio, D., Garai, M., Granzotto, N., Di Bella, A., Scamoni, F., Depalma, M., Marescotti, C., Serpilli, F., Lori, V., Nataletti, P., Annesi, D., Moschetto, A., Baruffa, R., De Napoli, G., D'Angelo, F., and Di Filippo, S. (**2020**). "Towards more reliable measurements of sound absorption coefficient in reverberation rooms: An Inter-Laboratory Test," Appl. Acoust. **165**, 107298.
Thiele, R. (**1953**). "Richtungsverteilung und Zeitfolge der Schallrückwürfe in Räumen" ("Directional distribution and temporal sequence of reflections in rooms"), Acustica **3**(4), 291–302.
Thomasson, S.-I. (**1980**). "On the absorption coefficient," Acustica **44**(4), 266–273.
Venzke, G., and Dämmig, P. (**1961**). "Measurement of diffuseness in reverberation chambers with absorbing material," J. Acoust. Soc. Am. **33**(12), 1687–1689.
Williams, E. G. (**1999**). *Fourier Acoustics*, 1st ed. (Academic Press, San Diego, CA).
Zotter, F. (**2009**). "Sampling strategies for acoustic holography/holophony on the sphere," in *Proceedings of the International Conference on Acoustics NAG/DAGA 2009*, Rotterdam, The Netherlands (March 23–26, 2009) [German Acoustical Society (DEGA), Berlin, Germany], pp. 1107–1110.